Hydrogen Evolution Reaction by Atomic Layer-Deposited MoN_x on Porous Carbon Substrates: The Effects of Porosity and Annealing on Catalyst Activity and Stability

Rahul Ramesh,[a] Sandesh Y. Sawant,[b] Dip K. Nandi,[a] Tae Hyun Kim,[a] Deok Hyun Kim,[a] Seung-Min Han,[a] Yujin Jang,[c] Myoung Gyu Ha,[c] Moo Hwan Cho,[b] Taeho Yoon,[b] and Soo-Hyun Kim*[a]

Molybdenum-based compounds are considered as a potential replacement for expensive precious-metal electrocatalysts for the hydrogen evolution reaction (HER) in acid electrolytes. However, coating of thin films of molybdenum nitride or carbide on a large-area self-standing substrate with high precision is still challenging. Here, MoN_x is uniformly coated on carbon cloth (CC) and nitrogen-doped carbon (NC)-modified CC (NCCC) substrates by atomic layer deposition (ALD). The as-deposited film has a nanocrystalline character close to amorphous and a composition of approximately Mo_2N with significant oxygen contamination, mainly at the surface. Among the as-prepared ALD-MoN_x electrodes, the MoN_x/NCCC has the highest HER activity (overpotential $\eta \approx 236$ mV to achieve 10 mA cm^{-2}) owing to the high surface area and porosity of the NCCC substrate. However, the durability of the electrode is poor, owing to the poor adhesion of NC powder on CC. Annealing MoN_x/NCCC in H_2 atmosphere at 400 °C improves both the activity and durability of the electrode without significant change in the phase or porosity. Annealing at an elevated temperature of 600 °C results in formation of a Mo_2C phase that further enhances the activity ($\eta \approx 196$ mV to achieve 10 mA cm^{-2}), although there is a huge reduction in the porosity of the electrode as a consequence of the annealing. The structure of the electrode is also systematically investigated by electrochemical impedance spectroscopy (EIS). A deviation in the conventional Warburg impedance is observed in EIS of the NCCC-based electrode and is ascribed to the change in the H^+ ion diffusion characteristics, owing to the geometry of the pores. The change in porous nature with annealing and the loss in porosity are reflected in the EIS of H^+ ion diffusion observed at high-frequency. The current work establishes a better understanding of the importance of various parameters for a highly active HER electrode and will help the development of a commercial electrode for HER using the ALD technique.

Introduction

As the effect of global warming has become more prominent over the past few years, researchers around the world are seriously considering the option of a hydrogen-based economy. Electrochemical water splitting is an efficient method for the production of hydrogen. However, several challenges need to be overcome before its large scale implementation. The most important are the higher overpotential (η) for the hydrogen evolution reaction (HER) and oxygen evolution reaction (OER), and the high cost of the catalysts.[1–4] The materials that are currently used as catalysts in acidic electrolyzers are mainly platinum-based (at the cathode, HER) and iridium–ruthenium composites (at the anode, OER).[3,4] Therefore, a significant amount of research effort has been made to develop new materials as cost-effective alternatives to the current precious metal catalysts for HER and OER. Currently, several alternative materials have been found to be active for HER and a significant improvement in the reduction of precious metal content has been achieved for OER catalysts.[5–8] Among alternative catalysts for HER, the performance of Mo-based catalysts is the most attractive. The reported activities of some Mo-based materials are very close to that of the state-of-art Pt.[11–19] Prominent among such materials are MoS_2, Mo_2C, and Mo_2N.[9–17] These catalysts have been synthesized by various synthesis techniques, such as hydrothermal synthesis, sol–gel processes, and chemical vapor deposition.[9–17] The major issue associated with carbides and nitrides is the difficulty in synthesizing the materials in pure form.[14–18] The extreme reaction conditions (elevated temperature and pressure) required for the synthesis

[a] Dr. R. Ramesh, Dr. D. K. Nandi, T. H. Kim, D. H. Kim, S.-M. Han, Prof. S.-H. Kim
School of Materials Science and Engineering
Yeungnam University, Gyeongsan, Gyeongbuk 38541 (Republic of Korea)
E-mail: soohyun@ynu.ac.kr

[b] Dr. S. Y. Sawant, Prof. M. H. Cho, Prof. T. Yoon
School of Chemical Engineering, Yeungnam University
Gyeongsan, Gyeongbuk 38541 (Republic of Korea)

[c] Y. Jang, Dr. M. G. Ha
Korea Basic Science Institute (KBSI), Busan Center
Busan Metropolitan City, Jinsa-dong, Gangseo-gu 46742 (Republic of Korea)

Supporting information [including detailed experimental procedures, SEM image of ALD-MoN_x on a SiO_2-Si substrate, physical characterizations (SEM images and XPS analysis) and electrocatalytic performances (electrochemical impedance analysis) of ALD-MoN_x on NCCC and CC substrate] and the ORCID identification number(s) for the author(s) of this article can be found under: https://doi.org/10.1002/cssc.202000350.

also limits the porosity and surface area of the fabricated electrodes.

Apart from the cost of the catalysts, the electrode fabrication procedure also creates additional challenges such as adhesion of the catalysts for better stability in hydrogen-gas-evolving conditions and maintaining good electrical conductivity and a large active surface area during the operation without compromising on the activity and durability.[18] Typically, mixing of the catalysts with a polymer binder and conducting carbon during the fabrication of the electrode is essential to improve the stability. However, this still limits the conductivity and the availability of the active surface area. The most common substrate used for an electrode in the HER is carbon cloth (CC). The CC substrate has relatively good electrical conductivity and is fairly stable in acidic conditions. Furthermore, CC is readily available and inexpensive. However, the surface area of bare CC is limited to a few centimeters per gram, which is adequate for a Pt-based electrode but is not sufficient for a non-Pt-based electrode, which requires a higher amount of material to obtain a similar performance. Several modification strategies have been adopted to increase the active surface area of CC as well as its rigidity, such as the incorporation of nitrogen or coating with nitrogen-doped carbon (NC) powder.[19,20] These alterations are quite effective at improving the specific surface area by creating a highly porous and rough surface on the carbon fiber. However, the practical application of these electrodes is still limited because of their poor durability.

The challenges associated with the synthesis of high-surface-area and porous molybdenum-based carbide and nitride electrodes can be overcome by using atomic layer deposition (ALD), which can effectively coat a thin film with excellent uniformity and conformality on a high-surface-area porous substrate at relatively low temperatures.[21–23] Furthermore, ALD can be used for precise control of the thickness of the coating, which is beneficial for electrode fabrication because an unnecessarily thicker active material not only adversely effects the electrical conductivity of the electrode but might also influences the catalytic activity as the electrocatalytic process is a surface-restricted phenomenon. Therefore, ALD is beneficial for the fabrication of free-standing large area electrodes for practical implementation. However, the properties of ALD-prepared molybdenum-based catalysts for HER, such as the activity of different phases, the influence of porosity, post-annealing, and the effect of these parameters on the durability of the electrode are not well documented in the literature. Therefore, understanding these factors is pivotal for the design of highly active and durable Mo-based electrodes for acidic HER as alternatives to precious Pt-based catalysts.

Results and Discussion

Synthesis of the NCCC substrate and MoN_x deposition by ALD

The coating of NC powder on carbon cloth is a well-established method to improve the active area of CC and enhance its conductivity.[19] The modification creates a highly porous surface.[20] In the rest of the manuscript, the surface area from this highly porosity resulting from NC powder coating on CC is designated as Type B contribution. The micrometer scale fibers in the CC make a Type C contribution. This assignment is also consistent with the active surface area induced by those characteristics. A Type C contribution only has a small effect on the enhancement of the surface area (the active surface area of bare carbon cloth), whereas a Type B contribution significantly enhances the surface area (the active surface area of NCCC). The nanometer-scale roughness of the surface is the most dominant factor that contributes to the overall surface area and hence is considered as a Type A contribution. The different types of contributions to the overall surface area of the electrode is schematically represented in Figure 1.

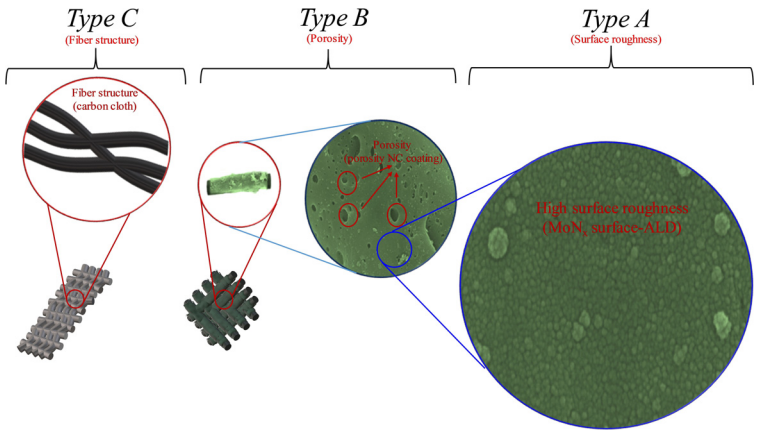

Figure 1. Schematic representation of various constituents on the electrode surface.

ALD of MoN_x is well established in the literature. However, the coating on a substrate with an extremely high surface area (such as the NCCC) owing to its significant amount of porosity (varying shapes and dimensions) and roughness is not trivial and, to the best of our knowledge, has not been attempted so far. The ALD technique is extensively used to grow various active compounds on different substrates for applications such as Cu diffusion barrier, energy storage devices, and electrocatalysis.[21–28] Recently, ALD has been explored as a fabrication technique for the preparation of various active materials on a highly porous substrate for application in fields such as Li-ion batteries and supercapacitor.[29–33] However, the deposition of MoN_x on CC or NCCC has not been reported and studied as a catalyst for HER. The self-limiting growth kinetics, the linearity of growth with ALD cycles and the temperature window for ALD-MoN_x using $Mo(CO)_6$ and NH_3 has been previously established by our group: The results indicated that the ideal ALD conditions occurs only in a very narrow temperature range of 200–215 °C on a SiO_2/Si substrate.[21–23] The number of ALD

cycles for the coating of a MoN_x thin film on CC and NCCC substrates was chosen to be 700 cycles to obtain a uniform thin film with a thickness of approximately 25–30 nm based on our previous study.[21–23] A schematic representation of the synthesis of the electrode is shown in Figure S1 (Supporting Information), and the conditions used during NCCC preparation, ALD-MoN_x coating, and heat-treatment are tabulated in Table S1.

Phase, morphology, and composition of the electrode

Initially, the thickness and composition of the MoN_x film were analyzed using cross-sectional SEM imaging and energy-dispersive X-ray spectroscopy (EDS) analysis of the MoN_x film on a SiO_2-Si wafer (Figure S2). The thickness of film grown with 700 ALD-cycles was approximately 25–30 nm, and the final composition of the film was approximately $Mo_{0.5}N_{0.25}O_{0.25}$ from the EDS analysis. However, the oxygen was mostly concentrated on the top surface and in the near-surface region of the film compared with the bulk. The ALD-growth kinetics, growth rate, and the composition of the ALD-MoN_x film have been extensively investigated and are described in our previous work.[21–23]

The structure and phase of the as-deposited MoN_x film on NC-powder-coated carbon cloth (MoN_x/NCCC), and that of the sample annealed in a hydrogen atmosphere at 400 °C (MoN_x/NCCC-400) and 600 °C (MoN_x/NCCC-600) were analyzed by XRD spectroscopy (Figure 2a). The post-annealing temperatures were chosen according to two important criteria; the Mo_2C formation temperature (by the reaction of carbon and molybdenum compounds, which is ca. 550 °C) and the temperature at which no significant morphological change happens in the electrode, but a possible reduction of surface oxides is expected.[34,35] Therefore, 600 °C and 400 °C were chosen for the post-annealing of the electrode. The broad peak at 2θ of 25° was attributed to the (002) plane of graphitic carbon and this peak was observed for all the samples. No peak other than that of graphitic carbon was evident in the XRD pattern of the MoN_x/NCCC electrode, which indicated that the as-deposited MoN_x film was amorphous. However, close examinations of the pattern revealed a minor hump at approximately 35–40° 2θ. From the standard XRD patterns (JCPDS reference code 00-025-1368), it can be interpreted that the minor hump in the case of MoN_x/NCCC might be from the Mo_2N phase. This also reflects the nanocrystallinity of the predominantly amorphous as-deposited film. This observation was in good agreement with MoN_x films that were deposited under similar conditions on either SiO_2/Si or Ni-foam substrates.[21–23] Furthermore, the annealing in a H_2 atmosphere at 400 °C had a minimal influence on the phase of ALD-MoN_x. However, the minor hump observed at 35–40° (Mo_2N 111) was much clearer and apparent. Therefore, the heat-treatment at 400 °C in a H_2 atmosphere slightly increased the crystalline nature of the film. Annealing of the as-deposited sample at a higher temperature (600 °C) resulted in the appearance of sharp peaks in the XRD patterns, which were assigned to Mo and β-Mo_2C phases (JCPDS reference codes 01-089-5023 and 01-011-0680, respectively). The decomposition of molybdenum nitrides to pure metal by releasing N_2 happens above 600 °C for the crystalline Mo_2N phase, whereas for amorphous MoN_x the nitrogen release might start at a slightly lower temperature.[34] Furthermore, the presence of a reducing atmosphere during annealing might reduce this reduction temperature of MoN_x to Mo. On the other hand, the formation of a Mo_2C phase was most probably caused by the presence of carbon in the NC powder.[35]

The oxidation state of molybdenum and the surface composition of the electrode were identified by X-ray photoelectron spectroscopy (XPS) analysis. The complete XPS survey spectra of bare CC, NCCC, MoN_x/CC, MoN_x/NCCC, MoN_x/CNCC-400, and MoN_x/CNCC-600 electrode are shown in Figure S3; peaks attributed to carbon, oxygen, molybdenum, and nitrogen were evident in the survey spectra. The deconvoluted high-resolution individual peak of Mo 3d of molybdenum in the MoN_x sample on the NCCC substrate is shown in Figure 2b. The Mo 3d spectrum from molybdenum foil (taken after 60 s Ar ion etching to remove surface oxides) and MoN_x/CC are shown in Figure S4. The binding energy (BE) values for $3d_{5/2}$ from Mo^0 and Mo^{+4}, respectively, were 228.23(±0.2) eV, and 229.7(±0.2) eV (Figure S4). The $3d_{5/2}$ peaks at 232.7(±0.2) eV and 231.1(±0.2) eV matched with reported BE values for +6 and +5 oxidation state, respectively, of molybdenum.[21,36,37] Apart from the above-mentioned peaks, the as-deposited MoN_x had one more peak (Mo $3d_{5/2}$ peak at 229(±0.2) eV) in between the BE values expected for Mo^{+2} and Mo^{+4} oxidation state (Figure 2b and S4) and was assigned to $Mo^{+\delta}$ oxidation state. This peak was from MoN_x phase in the case of MoN_x/CC, MoN_x/NCCC, and MoN_x/NCCC-400 samples.[21,37,38] Annealing the sample at 400 °C did not significantly alter the peak positions. However, the fraction of $Mo^{+\delta}$ significantly increased, and consequently, the fraction of Mo in higher oxidation states (+6 and +5) was reduced (Table S2). The heat-treatment at an elevated

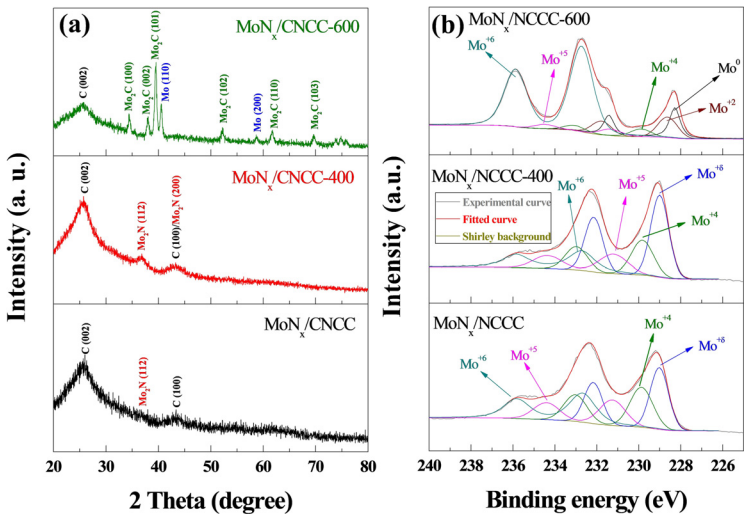

Figure 2. (a) XRD patterns and (b) Mo 3d XPS spectra of MoN_x/NCCC, MoN_x/NCCC-400, and MoN_x/NCCC-600.

temperature (600 °C) resulted in the appearance of peaks at BEs corresponding to Mo^0 and Mo^{+2} owing to the formation of the β-Mo_2C phase; a similar distribution of oxidation states has been reported for Mo_2C.[14,38] Significant contamination with the MoO_3 phase was observed in the spectrum; the peaks from Mo^{+6} became more prominent. However, only the formation of the Mo_2C and Mo phase was evident from the XRD analysis.

The SEM images of CC and NCCC are shown in Figure S5. The modification of CC with NC powder was apparent from the SEM images, and the porosity of the NCCC surface was clearly visible in the images. The NC powder appeared distinct. It formed a well-defined coating on CC. The NC coating, at the same time, also provided some extra growth of the material between the fibers to some extent, which should be considered as an advantage providing a further surface for depositing MoN_x. The NC coating formed through the carbothermal synthesis process was fairly uniform, well-adhered, and homogeneous on the CC substrate. The SEM images of NCCC clearly showed the extent of the porosity induced by NC modification. Pores with a wide range of sizes were generated through this modification. Microporous and nanoporous structures (pores, tunnels, holes) were clearly visible in the SEM images. Therefore, the NC-modified CC (NCCC) significantly increased the surface area and facilitated ALD onto the surface, eventually affecting the HER performance.

The SEM images of ALD-MoN_x-coated CC and NCCC, as well as the bare NCCC, are shown in Figure 3. A uniform coating of MoN_x film on CC was evident in the images of MoN_x/CC (Figure 3a and 3b). The MoN_x/CC (Figure 3b) surface appeared to be much rougher than that of the bare CC (inset to Figure 3b) owing to the uniform growth of the MoN_x nanoclusters consisting of several individual spherical particles on CC. Therefore, the analyses of these SEM images clearly reflect the potential of ALD for coating a thin film on a large area 3D substrate with excellent uniformity and conformality. The MoN_x coating on NCCC was not evident at a lower magnification (Figure 3e), but, similar to the MoN_x/CC, at higher magnification the MoN_x surface appeared (Figure 3f) with a very high degree of surface roughness when compared with that of bare NCCC (Figure 3c and 3d). The composition of the electrode and the elemental distribution of constituents were analyzed by EDS and EDS elemental mapping (Figure 4). The EDS mapping showed a uniform distribution of Mo and N on the carbon substrate. The carbon distribution was from the CC substrate and the carbothermal NC coating. The nitrogen from the MoN_x and NC coating contribute to the EDS signal; therefore, quantification from EDS mapping would be erroneous.

The SEM images of MoN_x/NCCC, MoN_x/NCCC-400, and MoN_x/NCCC-600 samples at low magnification are shown in Figure S6. Similar to that observed with MoN_x/NCCC, a uniform coating of N-doped carbon covered with a thin layer of ALD-MoN_x was evident for MoN_x/NCCC-400. There was also an indication of a minor change in the porosity of the coating but the low magnification SEM images were very similar to that of the as-prepared sample. The SEM images at high magnification (Figure 5a) confirmed the retention of the porosity after post-annealing at 400 °C. The images clearly revealed the highly porous structure of the electrode; pores with different dimensions were visible throughout the sample. However, the surface roughness (Figure 5b) of the MoN_x coating appeared to be slightly lower when compared with the as-deposited MoN_x/NCCC (Figure 3f). The SEM-EDS elemental mapping confirmed the presence of C, Mo, and N, which were still uniformly distributed throughout the sample after annealing at 400 °C (Figure S7). Annealing at 400 °C in a hydrogen atmosphere had a limited influence on the porosity of the electrode, whereas a slight decrease in the overall surface area arising from surface roughness was expected.

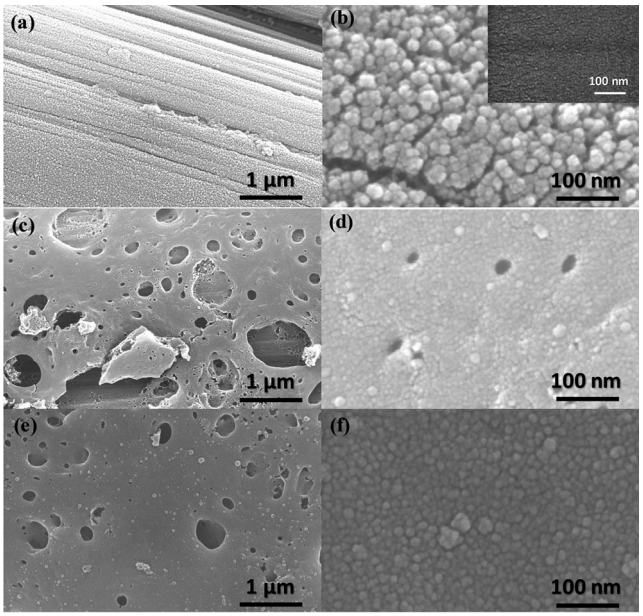

Figure 3. SEM images of (a, b) MoN_x/CC, (c, d) bare NCCC, and (e, f) MoN_x/NCCC electrodes at different magnifications. The inset in (b) is an SEM image of bare CC.

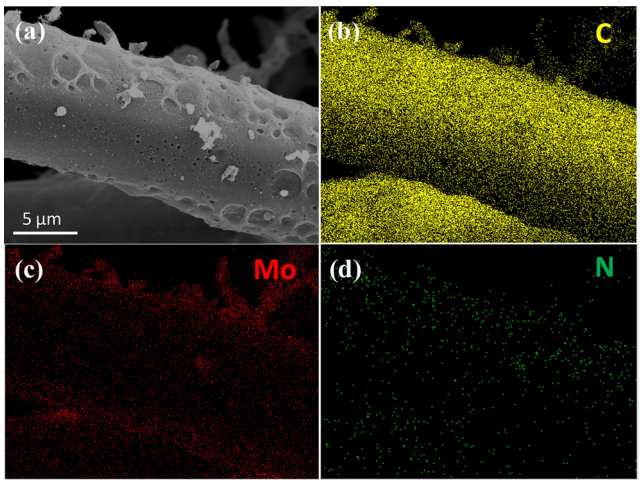

Figure 4. (a) SEM image of the ALD-MoN_x/NCCC electrode and the corresponding SEM-EDS elemental mapping for (b) carbon, (c) molybdenum, and (d) nitrogen.

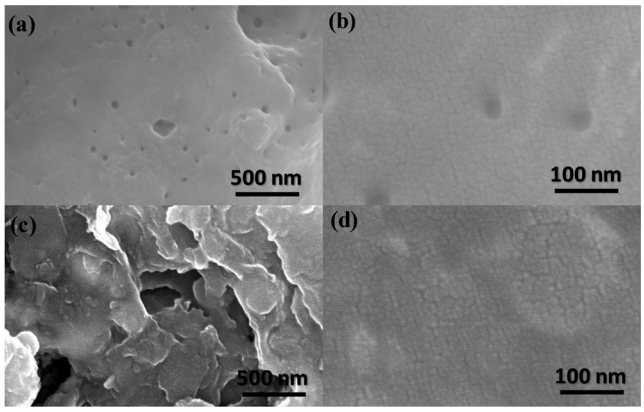

Figure 5. SEM images of (a, b) MoN_x/NCCC-400 and (c, d) MoN_x/NCCC-600 electrodes at different magnifications.

Severe aggregation (sintering of MoN_x/NC coating) of the coating was clearly evident in the SEM images (Figure S6c, and Figure 5c and 5d) of MoN_x/NCCC-600, resulting in the exposure of a significant portion of the carbon cloth fiber, which could be easily detected (Figure S6c). Even though there was a notable loss of surface coating of MoN_x–NC, the remaining coating was uniformly and homogeneously distributed on the CC. The SEM images further confirmed a significant loss of the porosity of the MoN_x/NCCC-600. The morphology of the surface changed from a highly porous structure to a scale-type structure (Figure 5c). Furthermore, the roughness of the surface was also significantly decreased after annealing at 600 °C (Figure 5d). Those changes in the morphology might be caused by the conversion of the as-grown material from the amorphous MoN_x phase (amorphous MoN_x with a notable amount of surface oxides) to a highly crystalline Mo and Mo_2C phase. This change in phase was clearly reflected in the XRD analysis. The SEM-EDS images and elemental mappings of the MoN_x/NCCC-600 electrode are shown in Figure S8; the images confirmed the uniform and homogeneous distribution of Mo, C as well as N throughout the sample even after annealing at 600 °C. The source of N might be the NC powder rather than MoN_x as the XRD analysis indicated the presence of only Mo and Mo_2C phase in the sample.

Electrochemical hydrogen evolution reaction activity and electrode stability.

Electrochemical HER performance of the bare CC, NCCC, and ALD-MoN_x-coated electrodes (MoN_x/CC and MoN_x/NCCC) before and after annealing were evaluated by linear sweep voltammetry (LSV) at a scan rate of 5 mV s^{-1} in a nitrogen-saturated 0.5 M H_2SO_4 electrolyte. The LSV curves without *iR* compensation and with *iR* compensation using the feedback method are shown in Figure 6a and Figure S9, respectively. The resistance for *iR* compensation was estimated from the EIS measurements, and the voltammograms were corrected for 85% *iR* drop. The bare CC had a non-convincing ability to catalyze the HER in the potential range used here, 0.0–0.6 V vs. RHE. However, the NCCC shows appreciable current owing to HER below −0.45 V. The reason for its slightly apparent activity might be owing to the increase in the surface area as well as the introduction of HER active sites by N-doping. It has been reported that the doping with heteroatoms with a higher electronegativity than carbon such as N, P, B, and S induces slight polarization of the adjacent carbon atom, thereby improving its H^+ ion adsorption and the HER activity.[39] The overpotential required for NCCC to achieve a current density of 10 mA cm^{-2} was approximately 514 mV. The introduction of ALD-MoN_x reduced the overpotential to approximately 402 and 236 mV for CC and NCCC, respectively. The apparent difference (ca. 166 mV) in overpotential of MoN_x/NCCC and MoN_x/CC was attributed to the high surface area of NCCC compared with that of CC. The above-mentioned conjecture is valid because of adopted synthesis/deposition strategy, that is, uniform and conformal coating of the entire surface of the electrode through ALD (both for CC and NCCC). This implies that the surface characteristics of both the electrodes are of the same nature. Therefore, the low overpotential observed with MoN_x/NCCC was attributed to the increased surface area and the consequent increase in the number of active sites.

Furthermore, annealing the as-prepared MoN_x/NCCC at 400 °C in a hydrogen atmosphere again pushed the HER overpotential to a lower value (ca. 222 mV at 10 mA cm^{-2}). This 14 mV drop was mainly owing to the reduction of surface oxides present on MoN_x during post-annealing in a hydrogen atmosphere at 400 °C, whereas most of the porous character of the as-prepared electrode was retained even after the annealing. Annealing at a relatively higher temperature of 600 °C resulted in a further drop in overpotential (ca. 196 mV). The electrode also exhibited very high performance resulting in an overpotential of approximately 465 mV (without *iR* correction) to reach a current density of 100 mA cm^{-2}. However, based on the SEM images, it was clear that there was also a subsequent loss in porosity and surface area owing to the annealing at elevated temperature. Therefore, the increased activity of the sample annealed at 600 °C was solely owing to the change in phase and composition of the catalysts. The formation of the Mo_2C phase, which has been reported to be highly active, was evident in the XRD analysis.[12–16] A similar trend was also observed with *iR*-corrected LSVs; the overpotentials at 10 mA cm^{-2} and 100 mA cm^{-2} for both *iR*-corrected and uncorrected voltammograms are tabulated in Table S3 and values from the literature for different Mo-based electrodes are also included in the table for comparison.[12,14,15,40–47] The results indicate that the HER activity of electrodes used in the current investigation is comparable with the values reported in the literature. However, most of the studies was performed with a rotating disc electrode set up,[15,40–42,44] whereas the catalytic activity in our study was evaluated in a free-standing electrode.

Tafel analysis can be used to identify the HER mechanism of the electrocatalysts as well as the relative activity of the electrode; according to the literature reports the HER occurs through three different individual steps.[48,49] Those are named Volmer, Heyrovsky, and Tafel reaction. The theoretically predicted Tafel slopes for the above-mentioned steps are

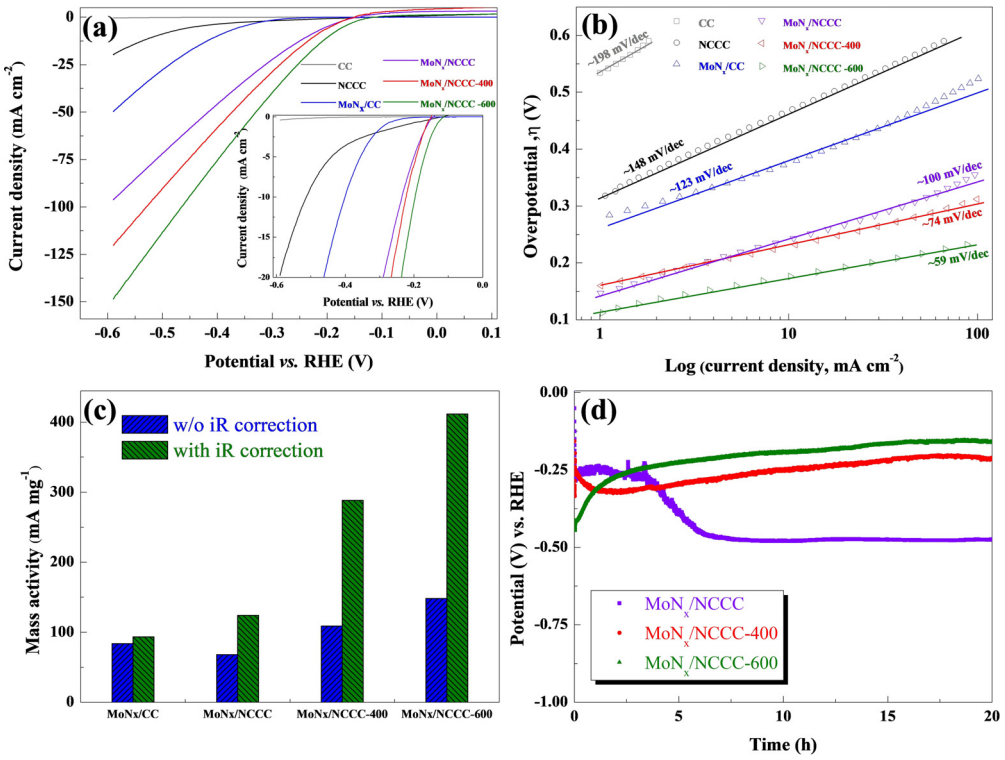

Figure 6. (a) Linear sweep voltammograms (without *iR* compensation) of CC, NCCC, MoN$_x$/CC, MoN$_x$/NCCC, MoN$_x$/NCCC-400, and MoN$_x$/NCCC-600 in 0.5 M H_2SO_4 at a potential sweep rate of 5 mV s^{-1}; the inset is an enlarged portion of the voltammograms. (b) Tafel plots (derived from the *iR*-compensated voltammograms), (c) mass normalized HER activity, and (d) chronopotentiometric (at 10 mA cm^{-2}) curve of the MoN$_x$/NCCC, MoN$_x$/NCCC-400, and MoN$_x$/NCCC-600 electrodes.

120 mV dec^{-1} (Volmer), 40 mV dec^{-1} (Heyrovsky), and 30 mV dec^{-1} (Tafel).[48,49] The Tafel plot derived from the *iR*-corrected LSVs are shown in Figure 6b; the apparent slope in the case of CC and NCCC was much higher than 120 mV dec^{-1}, which can be attributed to several reasons such as the coverage dependence of the rate-determining step, parallel reactions to the HER in the same potential window, and different transfer coefficient values for the deviation in the slope.[49] All the Mo-containing electrodes exhibited a Tafel slope of 120 mV dec^{-1} or in between 120 mV and 60 mV dec^{-1}, which indicated the Volmer–Heyrovsky reaction was the rate-determining step. Furthermore, the electrode tended to show an increased contribution from the Heyrovsky step with heat treatment. The lowest slope was observed for MoN$_x$/NCCC-600 (59 mV dec^{-1}) and is an indication of the high activity of the electrode.

The Mo-mass-normalized HER activity of MoN$_x$/CC, MoN$_x$/NCCC, MoN$_x$/NCCC-400, and MoN$_x$/NCCC-600 was also calculated by estimating the amount of molybdenum present through inductively coupled plasma-optical emission spectrometry (ICP-OES) analysis (Figure 6c and Table S4); the MoN$_x$/NCCC-600 had the maximum activity among all the electrodes. The loading of Mo on the electrode was estimated to be approximately 0.26–0.33 mg cm$^{-2}{}_{geo}$ for the NCCC-based electrode, whereas a much lower loading of approximately 0.019 mg cm$^{-2}{}_{geo}$ was observed for MoN$_x$/CC. The variation in the amount of molybdenum on CC and NCCC was due to the difference in their real surface area. More MoN$_x$ was deposited on NCCC than on CC with the same number of ALD cycles, owing to the surface self-limiting nature of ALD. Furthermore, the metal loading on the electrode by ALD was much lower when compared with the typically reported values using other fabrication methods (0.5 to 2 mg cm^{-2}).[15,44]

The durability of the electrode with good HER activity (LSVs) was assessed by performing chronopotentiometry (10 mA cm^{-2}) for 20 h in 0.5 M H_2SO_4 electrolyte. The potential versus time plot for the MoN$_x$/NCCC, MoN$_x$/NCCC-400, and MoN$_x$/NCCC-600 electrodes are shown in Figure 6d. A sudden increase in the potential from approximately 250 to 500 mV after approximately 4 h of electrolysis was observed for the MoN$_x$/NCCC electrode, which indicated a loss of HER activity owing to the instability of the electrode. The possible reason for the instability could be the loss of active sites/catalysts, that is, MoN$_x$. The loss of catalysts might happen owing to the poor adhesion of ALD-MoN$_x$ on NCCC or that of carbothermally coated NC on bare CC. To identify the reason for the loss of activity, chronopotentiometry analysis of the MoN$_x$/CC electrode was performed and compared with MoN$_x$/NCCC (Figure S10). If the cause of the activity loss was from the removal of the ALD-MoN$_x$ film from the substrate, then both the as-deposited electrodes (MoN$_x$/CC and MoN$_x$/NCCC) would have a similar stability profile. However, the MoN$_x$/CC had very good stability (no loss in operating potential) for 20 h. Therefore, the low stability of MoN$_x$/NCCC was due to the poor adhesion of the porous NC on the carbon cloth substrate. The SEM images of MoN$_x$/NCCC (Figure S11) after the chronopotentiometry further con-

firmed the above-mentioned conjecture; bare CC owing to the removal of MoN_x–NC coating was clearly evident (inset of Figure S11 d). Annealing the electrode at 400 °C or 600 °C in H_2 helped to improve the adhesion of MoN_x–NC on the CC substrate.

Electrochemical impedance spectroscopy (EIS) and pore geometry: Comparison of porosity from EIS and SEM images.

The morphology and porosity of the electrode are crucial factors for the electrochemical hydrogen evolution reaction because a higher porosity can enhance the active surface area of the electrode, which in turn increases the apparent HER activity. EIS has been widely used to characterize the nature of the porosity and the diffusion of ions and active species through pores of a variety of size and shapes.[50–58] The effect of the pore geometry on the impedance was first modeled by Keiser et al.,[53] and different groups have summarized numerical models or modifications to the Keiser et al. approach.[50–61] However, a direct correlation between the experimentally observed microstructure/porosity and the impedance response is rarely found in the literature.[59–61] In this work, we make an attempt to correlate the changes in the morphology/porosity caused by the annealing of the electrode at elevated temperature on the characteristic of the EIS spectra.

The EIS response for the MoN_x/NCCC, MoN_x/NCCC-400, and MoN_x/NCCC-600 electrode recorded at different HER overpotentials are shown in Figure 7. The EIS responses of bare CC, MoN_x/CC, and NCCC without any ALD-MoN_x coating are shown in Figure S12. The EIS data for the NCCC-based electrodes had features that were distinguishable from that of the CC-based electrodes; the spectra of MoN_x/NCCC (Figure 7 a) were dominated by an arc at the low-frequency region, which converged to a depressed semicircle with increasing overpotential, and was attributed to the kinetics of the HER. Furthermore, a curve almost parallel to the real axis (Z′ axis) at the high-frequency region was observed in the spectrum (inset to Figure 7 a). This curve (parallel to the X-axis) observed at a high-frequency was different from the 45° straight lines that are generally observed with a carbon-based electrode, and the difference was attributed to the pore-geometry of the electrode. For bare CC (Figure S12 a) and MoN_x/CC (Figure S12 c), this feature was not apparent, and the spectrum was composed of an arc at a lower overpotential and it converged into a depressed semicircle with an increase in the HER overpotential.

The EIS response of CC-based and NCCC-based electrodes is modeled with two different equivalent circuits (EC; Figure S13).[21,57,62] Both models use a constant-phase element instead of a pure capacitor to account for the heterogeneity of the surface.[63,64] For the CC-based electrode (CC and MoN_x/CC) both EC models give similar fitting results (Figure S14). However, in the case of the NCCC-based electrodes, the experimental data can only be perfectly fitted with the two constant-phase element circuit (Figure S15).

For MoN_x/NCCC (Figure 7 a), the low-frequency arc was clearly dependent on the applied potential (overpotential), whereas, the high-frequency portion exhibited potential independent characteristics, which further confirmed that the low-frequency characteristic corresponded to the kinetics of HER and the high-frequency curve was due to the porosity of the electrode. This was also reflected in the Bode plot shown in Figure 7 b, in which the spectra exhibit a constant low phase angle (5–10°) curve (almost parallel to the *x*-axis) in the frequency range of approximately 2–100 Hz, which corresponds to the diffusion of H^+ ions through the pores. At low frequency (1 Hz to 0.05 Hz) the Bode plots exhibited typical features (peak/curve with changing phase of Z at different frequencies) owing to the relaxation of surface electrochemical processes. Similar features were also observed with the NCCC electrode in its Nyquist and Bode representation (Figure S12 e and S12 f). The EIS analysis of MoN_x/NCCC-400 (Figure 7 c) also showed features similar to the as-deposited MoN_x/NCCC electrode. However, the high-frequency curve (inset to Figure 7 c) was slightly smaller in length for the annealed sample. This feature was much more apparent in the Bode plot (Figure 7 d), in which a smaller low phase curve (10–100 Hz) was present in the high-frequency region. The small change in the EIS feature of MoN_x/NCCC-400 when compared with the MoN_x/NCCC was attributed to the minor change in the porosity of the former electrode with annealing at 400 °C. The fitted parameters for the EIS spectra shown in Figure S12 and Figure 7 are tabulated in Table S5 and S6. The EIS response and the SEM images of the NCCC-based electrode suggested mostly pear-shaped or spherical pore geometry with distributed dimensions. However, modeling the exact shape and dimension from the EIS response is difficult owing to the various dimension and complexity of the pores and is beyond the scope of this article.[57] Heat-treatment at 600 °C resulted in further changes in the EIS response (Figure 7 e): the high-frequency curve was shorter in length and the semicircle from HER was reduced in size. This was also reflected in the Bode representation (Figure 7 f). In the Bode plot, the frequency at which HER relaxation occurred for MoN_x/NCCC-600 (recorded at an overpotential of 300 mV) was shifted to higher values compared with the MoN_x/NCCC-400, which was also at a higher frequency than for MoN_x/NCCC. This implied an improvement in HER activity with annealing; the MoN_x/NCCC-600 had better HER kinetics, owing to the formation of a more active surface (Mo_2C phase). The heat-treatment of the MoN_x/NCCC at 600 °C also resulted in the loss of the porous structure and consequently the high-frequency impedance response changed; this loss in the porous structure was also reflected in the SEM images (Figure S5 c).

The difference in the high-frequency (10–100 Hz) characteristic of the CC-based and NCCC-based electrode was attributed to the porosity of the NCCC electrode, which was again clearly reflected in the electrochemical surface area estimated from the double-layer capacitance (from the equivalent circuit fitting of the EIS spectra) at an η 300 mV for the various electrodes (Table S7).[65,66] The apparent double-layer capacitance is directly proportional to the real surface area of the electrode, and by normalizing with the theoretical specific capacitance (20 $\mu F\,cm^{-2}$), the surface area (Table S7) of the electrode can be estimated. The CC had a surface area of 0.0019 m^2, which is mainly owing to the fiber nature, and corresponds to the Type

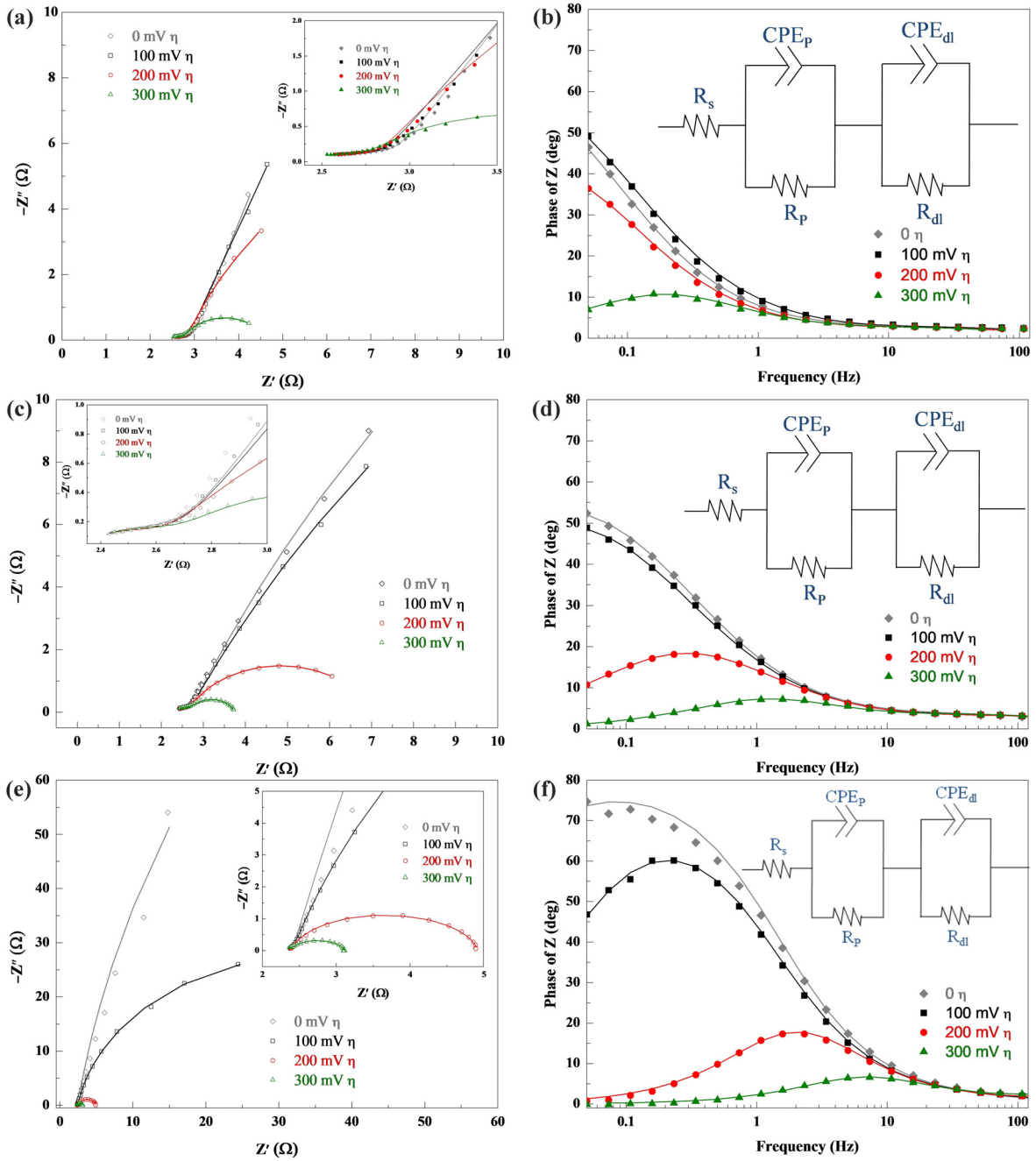

Figure 7. EIS spectra (Nyquist plots) of HER with (a) MoN_x/NCCC, (c) MoN_x/NCCC-400, and (e) MoN_x/NCCC-600 at different overpotentials in 0.5 M H_2SO_4. The insets in the figures are a magnified view of the spectra. The corresponding Bode representations are shown in (b), (d), and (f), with the equivalent circuit used to fit the experimental data displayed in the insets. The symbols represent the experimental data and the line represents the model data from the equivalent circuits.

C contribution, whereas, the NC coating significantly enhances the area to 1.264 m^2 owing to the Type B contribution of the porous structure of the electrode. The estimated surface area of MoN_x/CC was only 0.012 m^2. However, this was an order of magnitude higher than that of bare CC and was attributed to the much rougher surface of ALD-MoN_x compared with the carbon cloth surface. MoN_x/NCCC had a much higher surface area (1.891 m^2) than MoN_x/CC or bare NCCC, which was attributed to the significantly higher porosity of the modified NCCC substrate (Type B contribution) and surface roughness (Type A contribution) of MoN_x. Furthermore, the loss in the porosity with annealing was also clearly reflected in the estimated surface area values. The MoN_x/NCCC-400 electrode had a surface area of 1.116 m^2, whereas the significant loss of porosity of MoN_x/NCCC-600 resulted in a lower surface area (0.236 m^2).

The MoN_x/NCCC annealed at 600 °C had the highest HER activity and durability; the enhanced activity was attributed to the formation of the Mo_2C phase. Significant improvement in the stability of the electrode was accomplished by annealing of the as-deposited electrode at 400/600 °C, possibly owing to

the reduction of oxides and other functional groups on the NC, thereby improving the adhesion. Under the context of exploring highly efficient HER electrocatalysts for sustainable chemistry, the sample annealed at 600 °C, that is, the electrode that mainly consisted of the Mo_2C phase, seems most efficient relative to the other electrodes with higher electrode surface areas. Much better performance could be realized if the surface area of the electrode is also very high. The current work can be considered as the first attempt of a wider study and the follow-up objective will be the design of a Mo_2C/porous carbon cloth electrode using ALD.

Conclusions

The hydrogen evolution reaction was investigated over Mo-based catalysts supported on carbon cloth (CC) and NC-modified porous carbon cloth substrate (NCCC). The influences of the porosity and phase changes (induced by high-temperature annealing under hydrogen) of the electrode on the HER activity and the operational durability of the electrode were systematically evaluated by SEM imaging and EIS analysis. A highly porous NCCC substrate with a well-defined pore geometry was prepared by a novel carbothermal method and atomic layer deposition (ALD) was utilized to coat a uniform and conformal MoN_x thin film on the porous electrodes. Subsequently, the electrode was subjected to heat treatment at 400 or 600 °C in a H_2 atmosphere to induce temperature-dependent changes in the porous structure and phase. The as-deposited ALD-MoN_x thin film had a nanocrystalline character close to amorphous, and an overall composition of approximately $Mo_{0.5}N_{0.25}O_{0.25}$. Annealing at 400 °C did not significantly alter the porosity or phase of the thin film, whereas annealing at 600 °C resulted in a huge reduction in the porosity and a complete transformation of the amorphous MoN_x phase to crystalline Mo_2C and Mo phase. The apparent HER activity of the as-deposited MoN_x increased with the porosity of the substrate; MoN_x/NCCC had the highest activity. Annealing at 400 °C resulted in a reduction of surface oxides, which enhanced the HER activity. However, the increase in the HER activity of the sample annealed at 600 °C mainly resulted from a change in the phase of the MoN_x film to Mo_2C. The as-deposited electrode (MoN_x/NCCC) had reduced durability, owing to the poor adhesion of porous MoN_x–NC on the CC substrate. Considerable improvement in the stability of the electrode was observed after annealing. Finally, the apparent EIS profile of the porous electrode and its influence on the pore geometry, as well as the change in the EIS response with the loss of porosity owing to annealing was established. A deviation in the conventional Warburg impedance was observed in the EIS for the NCCC-based electrode and was ascribed to the change in H^+ ion diffusion characteristics, owing to the geometry of the pores. The current study provides valuable information about the influence of the phase and porosity of Mo-based catalysts towards HER, which will assist the development of more active electrodes for commercial hydrogen production through electrochemical water splitting.

Experimental Section

Preparation of NCCC substrate and MoN_x coating by atomic layer deposition

The preparation of the NCCC substrate was performed by a high-temperature carbothermal method; a detailed procedure is provided in the Supporting Information. A uniform thin film of MoN_x on the high-surface-area NCCC substrate was deposited at 225 °C by ALD (700 cycles) using the Lucida-M100 ALD reactor with molybdenum hexacarbonyl and ammonia gas as precursor and reactant, respectively. The deposition conditions were the same as those in an earlier report for MoN_x thin film by our group.[21–23] To prevent the sample loss during the vacuum deposition, owing to the light weight of the materials, the samples were attached to the sample holder (generally a silicon wafer) by using a heat-resistant polymer tape. For comparison, the commercial bare CC (before the NC powder modification) and the SiO_2/Si substrate were also coated with MoN_x film under similar conditions.

The as-prepared samples (abbreviated as MoN_x/NCCC) were subjected to annealing in a hydrogen atmosphere at two different temperatures to induce a structural, morphological, and phase change in the material. The annealing of the sample was performed in a rapid thermal annealing furnace at 400 or 600 °C for 30 min under a H_2 gas flow of 20 sccm and allowed to cool down to room temperature at a natural cooling rate. The annealed samples are abbreviated as MoN_x/NCCC-400 (heat-treated at 400 °C), and MoN_x/NCCC-600 (heat-treated at 600 °C).

Physical and electrochemical characterization

The samples were characterized by using different physical and compositional characterization techniques including XRD, SEM, EDS, XPS, and ICP-OES. The electrochemical characterizations were conducted at room temperature in a three-electrode setup with Ivium-n-Stat potentiostat/galvanostat using a graphite rod, Ag/AgCl (3 M KCl), and MoN_x-coated NCCC sample (1 $cm^2 g_{eo}^{-1}$) as the counter, reference, and working electrode, respectively. The detailed procedures and instrumentation for these characterizations are outlined in the Supporting Information.

Acknowledgements

This work was financially supported by a grant from the Advanced Technology Center (ATC) Program (#10077265) funded by the Ministry of Trade, Industry & Energy (MOTIE) of the Republic of Korea and also by the MOTIE (#10080651) and KSRC (Korea Semiconductor Research Consortium) support program for the development of future semiconductor devices. The precursor used in this study was provided by UP Chemical Co. Ltd., Korea.

Conflict of interest

The authors declare no conflict of interest.

Keywords: atomic layer deposition · electrocatalysis · electrochemical impedance spectroscopy · nitrides

[1] X. Li, X. Hao, A. Abudula, G. Guan, *J. Mater. Chem. A* **2016**, *4*, 11973–12000.

[2] R. Ramesh, S. Lee, S. Kim, J. Park, S. Lee, M. S. Kim, M. Baek, K. Yong, Y. Ye, J. Lee, *ChemistrySelect* **2018**, *3*, 5130 – 5137.
[3] M. Schalenbach, A. R. Zeradjanin, O. Kasian, S. Cherevko, K. J. J. Mayrhofer, *Int. J. Electrochem. Sci.* **2018**, *13*, 1173 – 1226.
[4] T. Reier, H. N. Nong, D. Teschner, R. Schlögl, P. Strasser, *Adv. Energy Mater.* **2017**, *7*, 1601275.
[5] X. Zou, Y. Zhang, *Chem. Soc. Rev.* **2015**, *44*, 5148 – 5180.
[6] X. Liang, L. Shi, Y. P. Liu, H. Chen, R. Si, W. S. Yan, Q. Zhang, G. D. Li, L. Yang, X. X. Zou, *Angew. Chem. Int. Ed.* **2019**, *58*, 7631 – 7635; *Angew. Chem.* **2019**, *131*, 7713 – 7717.
[7] E. Antolini, *ACS Catal.* **2014**, *4*, 1426 – 1440.
[8] L. C. Seitz, C. F. Dickens, K. Nishio, Y. Hikita, J. Montoya, A. Doyle, C. Kirk, A. Vojvodic, H. Y. Hwang, J. K. Norskov, T. F. Jaramillo, *Science* **2016**, *353*, 1011 – 1014.
[9] D. Merki, X. Hu, *Energy Environ. Sci.* **2011**, *4*, 3878 – 3888.
[10] J. D. Benck, T. R. Hellstern, J. Kibsgaard, P. Chakthranont, T. F. Jaramillo, *ACS Catal.* **2014**, *4*, 3957 – 3971.
[11] T. F. Jaramillo, K. P. Jørgensen, J. Bonde, J. H. Nielsen, S. Horch, I. Chorkendorff, *Science* **2007**, *317*, 100 – 102.
[12] H. Vrubel, X. Hu, *Angew. Chem. Int. Ed.* **2012**, *51*, 12703 – 12706; *Angew. Chem.* **2012**, *124*, 12875 – 12878.
[13] W.-F. Chen, J. T. Muckerman, E. Fujita, *Chem. Commun.* **2013**, *49*, 8896 – 8909.
[14] C. Wan, Y. N. Regmi, B. M. Leonard, *Angew. Chem. Int. Ed.* **2014**, *53*, 6407 – 6410; *Angew. Chem.* **2014**, *126*, 6525 – 6528.
[15] L. Ma, L. R. L. Ting, V. Molinari, C. Giordano, B. S. Yeo, *J. Mater. Chem. A* **2015**, *3*, 8361 – 8368.
[16] M. Miao, J. Pan, T. He, Y. Yan, B. Y. Xia, X. Wang, *Chem. Eur. J.* **2017**, *23*, 10947 – 10961.
[17] J. F. Callejas, C. G. Read, C. W. Roske, N. S. Lewis, R. E. Schaak, *Chem. Mater.* **2016**, *28*, 6017 – 6044.
[18] B. Bladergroen, H. Su, S. Pasupathi, V. Linkov, "Overview of Membrane Electrode Assembly Preparation Methods for Solid Polymer Electrolyte Electrolyzer" in *Electrolysis* (Eds.: V. Linkov, J. Kleperis), IntechOpen, **2012**, London, UK.
[19] W. Shen, W. Fan, *J. Mater. Chem. A* **2013**, *1*, 999 – 1013.
[20] S. Sawant, M. H. Cho, M. Kang, *Chem. Eng. J.* **2019**, *378*, 122158.
[21] R. Ramesh, D. K. Nandi, T. H. Kim, T. Cheon, J. Oh, S.-H. Kim, *ACS Appl. Mater. Interfaces* **2019**, *11*, 17321 – 17332.
[22] T. H. Kim, D. K. Nandi, R. Ramesh, S. Bonggeun, S.-H. Kim, *Chem. Mater.* **2019**, *31*, 8338 – 8350.
[23] D. K. Nandi, S. Sahoo, T. H. Kim, T. Cheon, S. Sinha, R. Ramesh, Y. Jang, J.-J. Bae, J. Heo, J.-J. Shim, S.-H. Kim, *Electrochem. Commun.* **2018**, *93*, 114 – 118.
[24] V. Miikkulainen, M. Leskelä, M. Ritala, R. L. Puurunen, *J. Appl. Phys.* **2013**, *113*, 021301.
[25] L. Hiltunen, M. Leskelä, M. Mäkelä, L. Niinistö, E. Nykänen, P. Soininen, *Thin Solid Films* **1988**, *166*, 149 – 154.
[26] M. Juppo, M. Ritala, M. Leskelä, *J. Electrochem. Soc.* **2000**, *147*, 3377 – 3381.
[27] V. Miikkulainen, M. Suvanto, T. A. Pakkanen, *Chem. Vap. Deposition* **2008**, *14*, 71 – 77.
[28] D. K. Nandi, U. K. Sen, D. Choudhury, S. Mitra, S. K. Sarkar, *ACS Appl. Mater. Interfaces* **2014**, *6*, 6606 – 6615.
[29] *Atomic Layer Deposition of Nanostructured Materials* (Eds.: N. Pinna, M. Knez), Wiley-VCH, Weinheim, Germany, **2011**.
[30] D. Gandla, D. Q. Tan, *Adv. Mater. Interfaces* **2019**, *6*, 1900678.
[31] M. Knez, K. Nielsch, L. Niinistö, *Adv. Mater.* **2007**, *19*, 3425 – 3438.
[32] X. H. Wang, C. Guan, L. M. Sun, R. A. Susantyoko, H. J. Fan, Q. Zhang, *J. Mater. Chem. A* **2015**, *3*, 15394 – 15398.
[33] S. Lu, H. Wang, J. Zhou, X. Wu, W. Qin, *Nanoscale* **2017**, *9*, 1184 – 1192.
[34] Z. Wei, Q. Xin, P. Grange, B. Delmon, *J. Catal.* **1997**, *168*, 176 – 182.
[35] M. Kiniger, C. Eisenmenger-Sittner, J. Hell, B. Schwarz, H. Hutter, S. Puchner, *Surf. Interface Anal.* **2008**, *40*, 786 – 789.
[36] J.-G. Choi, L. T. Thompson, *Appl. Surf. Sci.* **1996**, *93*, 143 – 149.
[37] G.-T. Kim, T.-K. Park, H. Chung, Y.-T. Kim, M.-H. Kwon, J.-G. Choi, *Appl. Surf. Sci.* **1999**, *152*, 35 – 43.
[38] K. Oshikawa, M. Nagai, S. Omi, *J. Phys. Chem. B* **2001**, *105*, 9124 – 9131.
[39] W. Zhou, J. Jia, J. Lu, L. Yang, D. Hou, G. Li, S. Chen, *Nano Energy* **2016**, *28*, 29 – 43.
[40] Y. Zhu, G. Chen, X. Xu, G. Yang, M. Liu, Z. Shao, *ACS Catal.* **2017**, *7*, 3540 – 3547.
[41] Y.-J. Song, Z.-Y. Yuan, *Electrochim. Acta* **2017**, *246*, 536 – 543.
[42] A. Morozan, V. Goellner, A. Zitolo, E. Fonda, B. Donnadieu, D. Jones, F. Jaouen, *Phys. Chem. Chem. Phys.* **2015**, *17*, 4047 – 4053.
[43] W.-F. Chen, S. Iyer, S. Iyer, K. Sasaki, C.-H. Wang, Y. Zhu, J. T. Muckerman, E. Fujita, *Energy Environ. Sci.* **2013**, *6*, 1818 – 1826.
[44] D. H. Youn, S. Han, J. Y. Kim, J. Y. Kim, H. Park, S. H. Choi, J. S. Lee, *ACS Nano* **2014**, *8*, 5164 – 5173.
[45] K. Ojha, S. Saha, B. Kumar, K. S. Hazra, A. K. Ganguli, *ChemCatChem* **2016**, *8*, 1218 – 1225.
[46] W. F. Chen, C.-H. Wang, K. Sasaki, N. Marinkovic, W. Xu, J. T. Muckerman, Y. Zhu, R. R. Adzic, *Energy Environ. Sci.* **2013**, *6*, 943 – 951.
[47] C. Ge, P. Jiang, W. Cui, Z. H. Pu, Z. Xing, A. M. Asiri, A. Y. Obaid, X. Sun, J. Tian, *Electrochim. Acta* **2014**, *134*, 182 – 186.
[48] A. Lasia, "Hydrogen evolution reaction" in *Handbook of Fuel Cells* (Eds.: W. Vielstich, A. Lamm, H. A. Gasteiger, H. Yokokawa), Wiley, Hoboken, **2010**.
[49] T. Shinagawa, A. T. Garcia-Esparza, K. Takanabe, *Sci. Rep.* **2015**, *5*, 13801.
[50] A. Lasia, *Electrochemical Impedance Spectroscopy and its Applications*, Springer-Verlag, New York, **2014**.
[51] *Advances in Electrochemistry and Electrochemical Engineering* (Ed.: R. De Levie, P. Delahay), Wiley-VCH, Weinheim, **1967**.
[52] U. Tröltzsch, O. Kanoun, *Electrochim. Acta* **2012**, *75*, 347 – 356.
[53] H. Keiser, K. D. Beccu, M. A. Gutjahr, *Electrochim. Acta* **1976**, *21*, 539 – 543.
[54] R. De Levie, *Electrochim. Acta* **1963**, *8*, 751 – 780.
[55] I. Raistrick, *Electrochim. Acta* **1990**, *35*, 1579 – 1586.
[56] K. Eloot, F. Debuyck, M. Moors, A. P. Van Peteghem, *J. Appl. Electrochem.* **1995**, *25*, 326 – 333.
[57] C. Hitz, A. Lasia, *J. Electroanal. Chem.* **2001**, *500*, 213 – 222.
[58] R. Jurczakowski, C. Hitz, A. Lasia, *J. Electroanal. Chem.* **2004**, *572*, 355 – 366.
[59] C. González-Buch, I. Herraiz-Cardona, E. Ortega, J. García-Antón, V. Pérez-Herranz, *J. Appl. Electrochem.* **2016**, *46*, 791 – 803.
[60] D. Cericola, M. E. Spahr, *Electrochim. Acta* **2016**, *191*, 558 – 566.
[61] S. J. Cooper, A. Bertei, D. P. Finegan, N. P. Brandon, *Electrochim. Acta* **2017**, *251*, 681 – 689.
[62] R. D. Armstrong, M. Henderson, *J. Electroanal. Chem. Interf. Electrochem.* **1972**, *39*, 81 – 90.
[63] G. J. Brug, A. L. G. van den Eeden, M. Sluyters-Rehbach, J. H. Sluyters, *J. Electroanal. Chem. Interfacial Electrochem.* **1984**, *176*, 275 – 295.
[64] J.-B. Jorcin, M. E. Orazem, N. Pébère, B. Tribollet, *Electrochim. Acta* **2006**, *51*, 1473 – 1479.
[65] B. Bera, T. Kar, A. Chakraborty, M. Neergat, *J. Electroanal. Chem.* **2017**, *805*, 184 – 192.
[66] R. K. Singh, R. Ramesh, R. Devivaraprasad, A. Chakraborty, M. Neergat, *Electrochim. Acta* **2016**, *194*, 199 – 210.

Manuscript received: February 9, 2020
Revised manuscript received: March 11, 2020
Accepted manuscript online: March 23, 2020
Version of record online: May 11, 2020